Title

Low-Profile and Low-Dispersion Artificial Impedance Surface in the UHF Band Based on Non-Foster Circuit Loading

Journal

IEEE Transactions on Antennas and Propagation, 64(7)

ISSN

0018-926X

Authors

Long, Jiang

Sievenpiper, Daniel F

Publication Date

2016-07-01

DOI

10.1109/tap.2016.2562658

Peer reviewed

Low-Profile and Low-Dispersion Artificial Impedance Surface in the UHF Band Based on Non-Foster Circuit Loading

Jiang Long, *Student Member, IEEE*, and Daniel F. Sievenpiper, *Fellow, IEEE*

***Abstract*— Conventional artificial impedance surfaces are too thick for practical use at ultrahigh frequencies (UHFs). Thin structures with passive capacitive loading are possible in the UHF band, but only with narrow bandwidth. This paper presents a non-Foster loaded artificial impedance surface to achieve low-profile and wide bandwidth simultaneously in the UHF band. The high resonant frequency associated with a thin structure is reduced by the synthesized non-Foster-type impedance load. For a demonstration, we designed a 5-mm-thick actively loaded surface for obtaining a high-impedance condition supporting slow transverse magnetic (TM) surface waves with a propagation index of 1.5, which corresponds to a 420-$j\Omega$ impedance surface. The non-Foster impedance is synthesized to be equivalent to −2.8 pF || −3.6 nH. Both the non-Foster impedance and the surface are fabricated and tested with a near-field measurement. The retrieved refractive index shows a constant TM propagation index of 1.5 over a bandwidth of 450–800 MHz, a 56% fractional bandwidth. By varying the biasing voltage of the non-Foster circuit, the impedance can be tuned from 250 to 420 $j\Omega$, while maintaining low dispersion over the same bandwidth.**

***Index Terms*— Broadband, dispersion, high-impedance surface, metamaterial, metasurface, non-Foster circuits, periodic structure.**

I. Introduction

AN ARTIFICIAL impedance surface is an electromagnetic structure that can be abstracted as a reactive surface impedance boundary, so that it is capable of supporting and interacting with the surface wave propagation [1], [2]. This has inspired many applications, such as surface wave waveguides [3], radar crosssection reduction [4], surface wave absorbers [5], and nonlinear metasurfaces [6]. It has been further applied to various antenna applications, including artificial magnetic conductors (AMCs) for antenna ground plane [7], antenna reflector [8], and decoupling of multiple antennas [9].

Impedance surfaces have generated so much interest primarily due to their low profile and the simplicity of fabrication, providing superiority over the conventional bulky metamaterials. However, artificial impedance surfaces become impractically thick when designed for the ultrahigh frequency (UHF) band. This can be seen from the basic principle of the artificial impedance surfaces. For a typical patch structure as shown in Fig. 1, looking from the top to the surface, the two patches can be modeled as a capacitor, and the substrate together with the ground forms a small section of short-circuited transmission line. Therefore, the surface impedance is equivalent to a shunt LC circuit. When operating near the resonant frequency, a reactive surface impedance is obtained and the surface supports bound surface waves. To achieve an impedance surface at UHF, the LC product should be large enough to provide a resonance at hundreds of megahertz. Using a large C is not a good approach, since it results in larger quality factor, Q, consequently, reducing the bandwidth. In contrast, sufficient L can be realized by increasing the thickness of the substrate, which is a possible approach and is even helpful in producing more bandwidth; nevertheless, this may lead to a thick structure that is no longer practical. Therefore, there is a tradeoff between the impedance surface thickness and the bandwidth, limiting the artificial impedance surface applications in the UHF band. In addition, the reactive impedance is always frequency dependent near the resonance, causing dispersion and consequently further limiting the bandwidth. Thus, it is necessary to find a solution for designing a low-profile and low-dispersion artificial impedance surface in the UHF band.

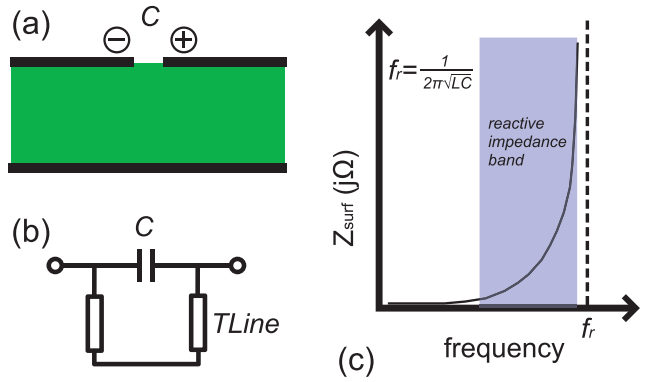

Fig. 1. Fundamental principle of the artificial impedance surfaces. (a) is the physical geometry of the impedance surface; (b) is the equivalent circuit; (c) shows the resultant surface impedance.

Many efforts have been directed at mitigating the tradeoff between the thickness and the bandwidth. Resistively loading a low-profile impedance surface is helpful to obtain broadband absorbers [10], [11], but this approach works only for absorber designs which are intended to absorb/attenuate the incoming

Manuscript received December 3, 2015; revised April 17, 2016; accepted April 28, 2016. Date of publication May 4, 2016; date of current version July 5, 2016. This work was supported by the National Science Foundation under Grant ECCS-1306055.

The authors are with the Department of Electrical and Computer Engineering, University of California at San Diego, La Jolla, CA 92093 USA (e-mail: jilong@ucsd.edu; dsievenpiper@eng.ucsd.edu).

Color versions of one or more of the figures in this paper are available online at http://ieeexplore.ieee.org.

Digital Object Identifier 10.1109/TAP.2016.2562658

waves. Tunable/reconfigurable high impedance surface (HIS) is another possible solution for designing a thin HIS that is capable of covering a large frequency bandwidth by continuously tuning the loaded elements (usually diodes) [12], [13]. However, this method does not provide wide instantaneous bandwidth as only small bandwidth can be achieved at each configuration. Alternatively, loading an artificial impedance surface with non-Foster circuits, which has been theoretically reported in [14], is a promising technology to resolve the bandwidth–thickness tradeoff, further increasing the bandwidth. There has been much research reported on broadband applications with non-Foster circuits [15]–[25]. For example, a broadband AMC has been measured in a coaxial transverse electromagnetic waveguide by loading the impedance surface with non-Foster negative inductors [21]. Although bandwidth is improved, the surface still has in-band dispersion, i.e., frequency-dependent surface impedance. Other work [16], [17] has demonstrated that the use of a negative inductor and capacitor combination can further increase the bandwidth of electrically small antennas, and our previous simulation showed that such an approach can also be applied to the design of a broadband reflection-type phase shifters [23] and artificial impedance surfaces [24].

In this paper, a low-profile artificial impedance surface is experimentally demonstrated by loading non-Foster impedance. Starting from a conventional 5-mm-thick impedance surface resonating at over 1 GHz, an optimized non-Foster-type frequency-dependent impedance, which is capable of producing a constant surface wave propagation index, is synthesized by the approach of sweeping the loading capacitance [16], [17]. The required non-Foster load, a shunt combination of -2.8 pF || -3.6 nH, is designed and integrated with the thin artificial impedance surface. The near-field measurement of the non-Foster impedance loaded surface presents a constant surface wave index of 1.5, corresponding to a 420-$j\Omega$ surface impedance, over 450–800 MHz, a fractional bandwidth (FBW) of 56%. By varying the biasing voltage of the non-Foster circuit, the achieved surface impedance can be tuned from 250 to 420 $j\Omega$, while maintaining the low dispersion and the same bandwidth.

This paper is organized as follows. Section II presents the synthesis approach for determining the desired non-Foster impedance in detail. An artificial impedance surface with such synthesized non-Foster impedance is demonstrated by both eigenmode and driven mode simulations in Section III. Section IV describes the non-Foster circuit design and the loaded impedance surface fabrication, and the measurement results are detailed and discussed in Section V. Section VI concludes this paper.

II. Synthesis of the Non-Foster Frequency-Dependent Impedance Loads

The primary goal of this design is to achieve a low-profile and low-dispersion artificial impedance surface for surface wave propagation in the UHF band. As an example for demonstrating the synthesis algorithm, we design a low-profile impedance surface supporting transverse magnetic (TM) surface waves with a refractive index of 1.5 around 500 MHz.

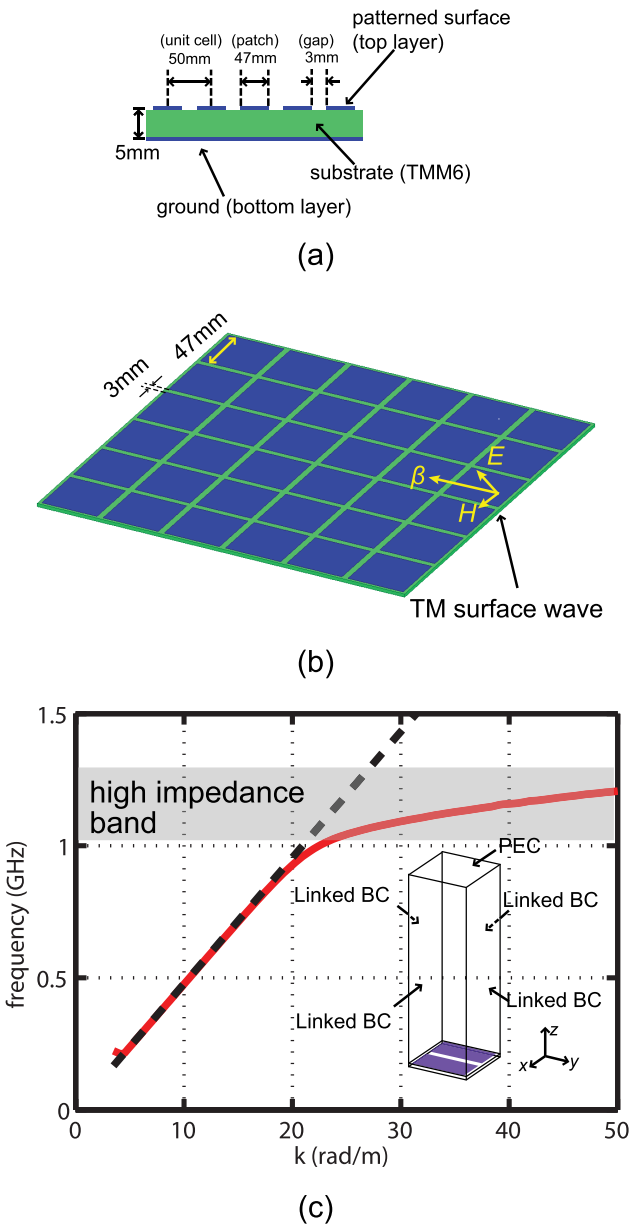

Fig. 2. Low-profile impedance surface dimension and its dispersion diagram without any loads. (a) and (b) Dimensions of the unit cell. (c) Dispersion diagram, with the description on the eigenmode simulation configuration.

At first, a conventional thin square patch-based impedance surface structure is chosen, as illustrated in Fig. 2(a) and (b). The dimension of the unit cell is 50 mm, with a 47-mm square patch and 3-mm gap between adjacent patches. The thickness of the Rogers TMM6 substrate ($\epsilon_r = 6$) is 5 mm. In this design, we are focused on TM surface waves. The eigenmode simulation configuration and its resulting dispersion curve are presented in Fig. 2(c). Linked boundary conditions (BCs) are used in the eigenmode simulation. The top face of the tall air box is set as a perfect electric conductor boundary for expediting the simulation while maintaining accuracy since the surface wave is well confined near the surface, and exponentially decays away from the surface.

The dispersion diagram in Fig. 2(c) implies that the resonant frequency is about 1.2 GHz, and it presents high impedance

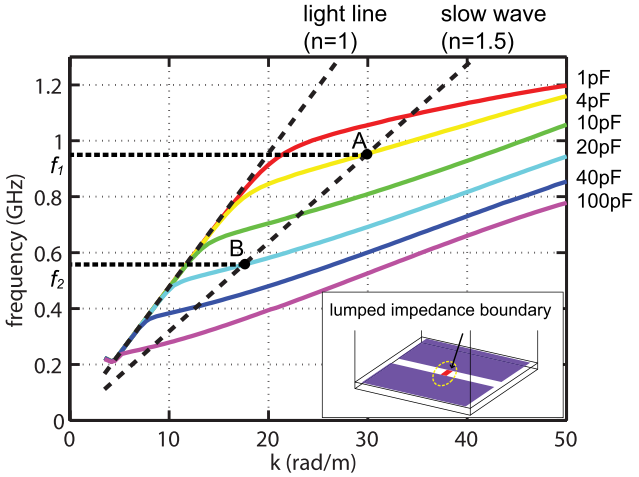

Fig. 3. Impedance surface with passive capacitance swept from 1 to 100 pF. Points A and B are the intersection of the swept dispersion curve and the ideal $n = 1.5$ slow wave dispersion curve.

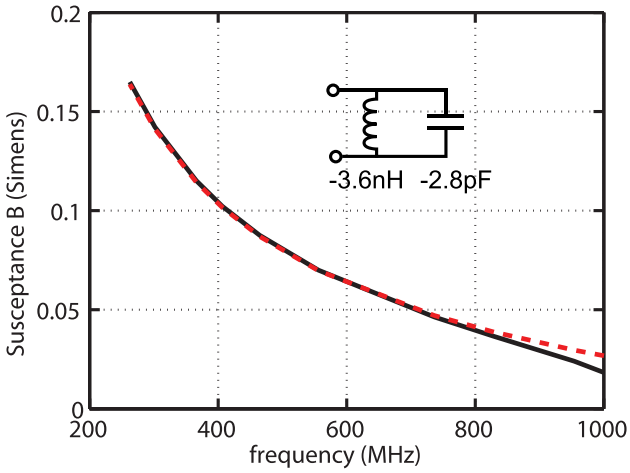

Fig. 4. Synthesized loading impedance (black solid curve) and its equivalent non-Foster element combination (red dotted curve).

from about 1 to 1.2 GHz, which is much higher than our target of 500 MHz. Since it is well known that loading a capacitance between the patches can reduce the resonant frequency, enabling the surface to work at a lower band [1], a lumped capacitance in the gap implemented with RLC boundary in HFSS is added and swept from 1 to 100 pF, as shown in the inset of Fig. 3. The eigenmode simulation results of the sweep are summarized in Fig. 3, from which it is evident that the resonant frequency is reduced by the loading capacitor. Furthermore, it is observed that different dispersion curves have been achieved with different loaded capacitances. In particular, the greater the loaded capacitance, the lower the resonance frequency.

With a goal of providing a dispersion curve with a constant index of 1.5, as shown by the dashed line in Fig. 3, the points on the targeted ideal $n = 1.5$ line intersecting with the swept dispersion curves, such as point A and B in Fig. 3, are of the most importance. In particular, point A indicates that a 10-pF capacitor is needed to load the impedance surface for achieving an $n = 1.5$ index at frequency f_1. Similarly, point B means that a 20-pF load is demanded for f_2. This can be further interpreted as how much susceptance is required for the load to achieve an $n = 1.5$ index at each frequency. Therefore, based on all the intersecting points, it is possible to derive a susceptance–frequency table to describe this required frequency-dependent load, with which the resulting dispersion curve of the loaded HIS passes through all of the intersecting points, lining up with the targeted ideal $n = 1.5$ dispersion curve. Since the intersecting points range from 200 to 1000 MHz, the synthesized dispersion curve can be expected to overlap with the targeted $n = 1.5$ curve over the bandwidth of 200–1000 MHz.

Such frequency-dependent susceptance is plotted as the solid curve in Fig. 4. Two points can be observed from Fig. 4.

1) The slope of the susceptance versus frequency is negative, clearly implying that this synthesized impedance is a non-Foster impedance [26].
2) It can be fitted by a shunt circuit of -3.6 nH and -2.8 pF (the dashed curve in Fig. 4), indicating that only a single non-Foster element such as a negative inductor is not enough for reducing the dispersion.

TABLE I
SYNTHESIZED NON-FOSTER IMPEDANCE SHUNT LUMPED EQUIVALENT

index	Z_{surf}	shunt L	shunt C
$n = 1.2$	$250\ j\Omega$	-4.1 nH	-3.4 pF
$n = 1.5$	$420\ j\Omega$	-3.6 nH	-2.8 pF

It should be noted that there is a slight difference between the LC fitted impedance and the synthesized impedance, which theoretically results in the deviation of the surface impedance from the targeted value. A more complicated circuit can fit the synthesized value better. Nevertheless, we still choose a simple LC combination to simplify the non-Foster circuit design. With the same manner, the frequency-dependent non-Foster impedance for $n = 1.2$ is also derived and summarized in Table I.

To summarize this section, a frequency-dependent load is synthesized by finding the intersecting points of the swept dispersion curves and the targeted ideal curves [16], [17]. This load is identified as a non-Foster impedance.

III. SIMULATION ON THE ARTIFICIAL IMPEDANCE SURFACE WITH THE SYNTHESIZED NON-FOSTER IMPEDANCE LOAD

As a demonstration, the 5-mm-thick impedance surface loaded with the previously synthesized frequency-dependent non-Foster impedance is simulated. Two simulation approaches are adopted: eigenmode simulation and driven mode simulation.

The eigenmode simulation model is the same as the inset of Fig. 3, with the lumped RLC boundary being configured as -3.6 nH || -2.8 pF. The driven mode simulation model is illustrated in Fig. 5(a). A 1-m-long non-Foster loaded surface composed of 20 unit cells is placed in a tall air box with three faces (top, front, and end faces) configured as radiation boundaries. A perfect magnetic conductor (PMC) is used for both left and right faces since only the TM surface wave is

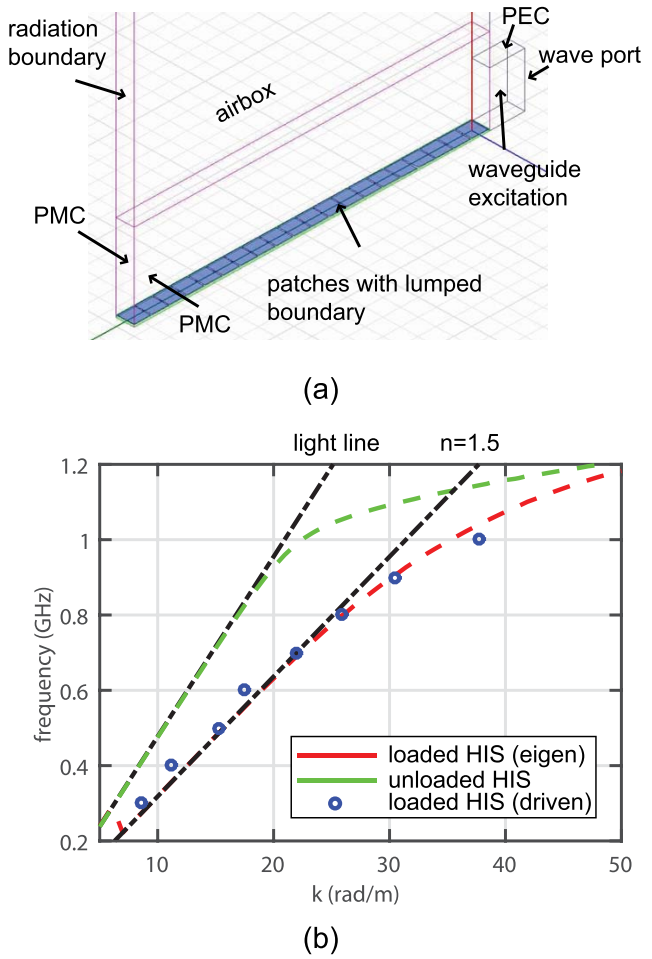

Fig. 5. Simulation demonstration of the impedance surface loaded with the synthesized impedance. (a) Driven mode simulation configuration. (b) Simulated results for both driven mode and eigenmode simulation, which is compared with the light line and the targeted $n = 1.5$ slow wave line. The dispersion curve of the unloaded impedance surface is appended for comparison.

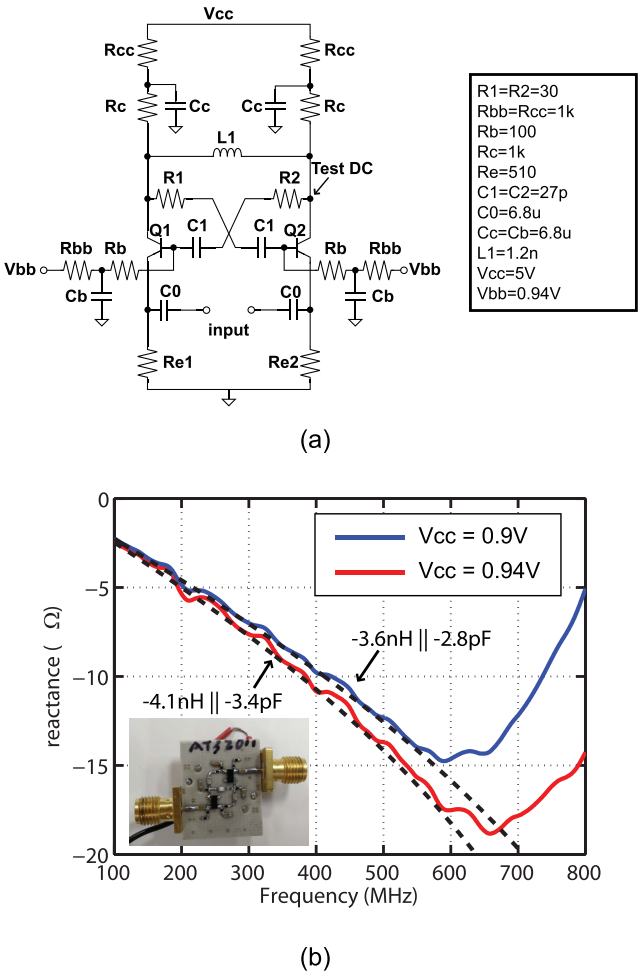

Fig. 6. Designed non-Foster circuit for the synthesized impedance. (a) Schematic and (b) its measurement results at 0.9 and 0.94 V are compared with the synthesized impedance. The measurement sample is shown in the inset of (b).

of interest. The non-Foster load in each unit cell is realized by a lumped boundary. A parallel-plate waveguide is utilized for exciting a vertically polarized plane wave, which is coupled to the surface as a TM surface wave mode. The phase progression along the longitudinal direction is extracted, from which the propagation constant at the excitation frequency is calculated. The excitation is swept in the frequency domain so that the dispersion information is obtained.

The simulated dispersion diagrams from both eigenmode and driven mode simulations are presented in Fig. 5(b). In eigenmode simulation, only the lowest TM mode is selected. Similarly, in the driven mode simulation, the TM mode is selected due to the use of the PMC BC, which prevents the incident wave from coupling into the TE surface wave mode. It can be seen that both results are consistent, confirming an almost constant $n = 1.5$ dispersion curve over a wide bandwidth, demonstrating that very low dispersion surface wave propagation is accomplished. Thus, it is demonstrated that with the synthesized non-Foster impedance load, the 5-mm-thick impedance surface is able to support a wideband dispersion-reduced $n = 1.5$ surface wave propagation.

IV. Non-Foster Impedance Design and the Loaded Artificial Impedance Surface Fabrication

The synthesized non-Foster impedance is designed based on Linvill's impedance converter circuit (NIC) [27]. In particular, since the circuit is intended to be loaded between the two adjacent patches, which possesses high impedance at low frequencies, the open circuit stable (OCS)-type NIC is adopted for the stability consideration. The circuit schematic and the electronic component values are illustrated in Fig. 6(a). As it is recommended that the transient frequency, f_t, of the transistor should be ten times larger than the operating frequency [25], Avago transistor AT32011 with the f_t of 10 GHz is adopted, which is optimized for UHF application. The two transistors are cross coupled, providing positive feedback. An inductor is connected between the collectors of the two transistors. This inductor, along with the biasing networks at the collectors, forms the parallel LC circuit for impedance conversion. In the OCS configuration, the output is at the two emitters, where two resistors are used for dc biasing. In addition, resistors in the cross-coupled loop are for controlling the loop gain for stability. Stability is one of the biggest challenges during the design phase. The μ-factor and Nyquist stability criteria

approaches are used in the frequency domain, and the transient simulations are adopted in the time domain to predict the stability [28], [29]. Since the method of simulating the stability has been being debated [30], these approaches are just for preliminary examination. The actual stability is tested in measurement with a spectrum analyzer (by examining any spurious spikes over dc to 10 GHz) and with an oscilloscope (by checking the time domain waveform) [20].

The non-Foster circuit is designed and fabricated on a 10×10 mm^2 printed circuit board (PCB) with 0.9-mm-thick Rogers RO4003C ($\epsilon_r = 3.4$) substrate as shown in the inset of Fig. 6(b). All the traces in the layout are kept short so as to avoid unwanted parasitics. The parasitics of the layout are modeled and extracted from HFSS for cosimulation, for predicting the frequency-domain performance and stability. The simulation first passed the transient test for stability, and we then calculated the input impedance with the frequency-domain simulation. The fabricated sample is also tested with a spectrum analyzer and an oscilloscope to ensure stability, and then measured in the frequency domain. The result after de-embedding is shown in Fig. 6(b), where it is confirmed that the fabricated non-Foster circuit possesses a susceptance very close to what is synthesized. In addition, by tuning the biasing voltage, both impedances needed for constant index of $n = 1.2$ and $n = 1.5$ are realized over a wide bandwidth.

The entire non-Foster impedance loaded surface is designed as shown in Fig. 7, where Fig. 7(a) illustrates how the surface and non-Foster circuit are configured. The unit cell is the same as depicted in Fig. 2(a). The non-Foster circuit is fabricated and attached to the other side of the impedance surface. The circuits and artificial impedance surface are sharing the same ground plane and connected through vias, so that not only are the parasitics minimized, but also the circuit components are immune to the impact from the impedance surface side, and the fabrication process is simplified as all electronic components are surface mounted on the bottom side. The ground is configured on the second layer from the top, providing an intact artificial impedance surface structure. The third layer is for dc bias routing, which is also an ac ground. Besides through hole vias connecting the non-Foster circuit to the patches, buried vias are used for connecting the ground on the second layer and the power network on the third layer to the non-Foster circuit on the bottom layer. A non-Foster loaded surface consisting of 7×10 unit cells is fabricated as shown in Fig. 7(b) and (c). The total thickness of the surface is about 5.9 mm.

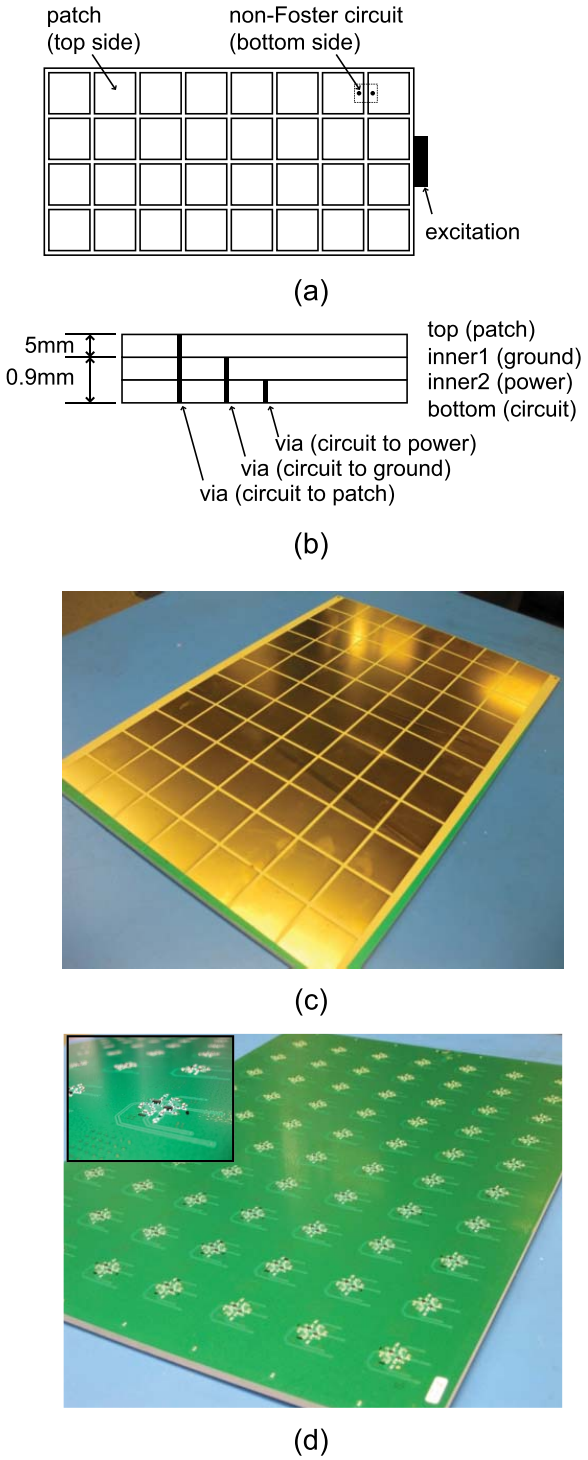

Fig. 7. Fabrication of the non-Foster loaded artificial impedance surface. (a) and (b) Entire PCB configuration. (c) and (d) Top and bottom sides of the fabricated sample.

V. Measurement and Discussion

The fabricated non-Foster loaded artificial impedance surface is measured with the near-field measurement approach, as illustrated in Fig. 8. Two fabricated 7×10 unit cell panels are cascaded and put underneath a vertically polarized high-impedance probe. A WR10 waveguide is used for excitation with the E-field oriented in the vertical direction. The probe is scanned in the horizontal plane to measure the relative magnitude and phase progression on the surface. When the non-Foster circuit is biased at 0.9 V, the measured E_z field distribution at 0.65 GHz is plotted in Fig. 9(a), demonstrating that the excited wave from the rectangular waveguide adapter is converted into a surface wave propagating along the surface. The apparent attenuation is due to the loss of the non-Foster loaded surface. The phase progression at the center line [see Fig. 9(a)] is extracted, unwrapped, and presented in Fig. 9(b). To find the propagation constant, the first-order linear fit

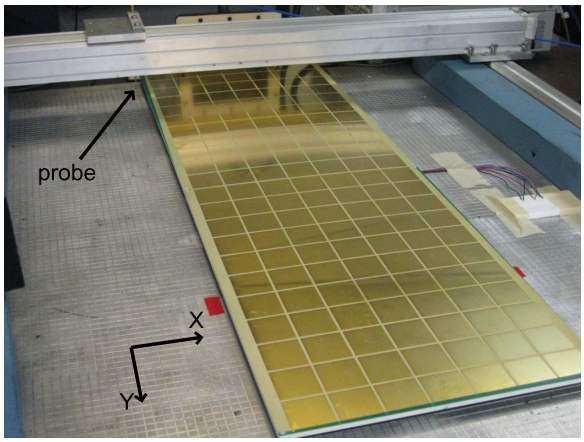

Fig. 8. Near-field measurement setup of the non-Foster loaded artificial impedance surface.

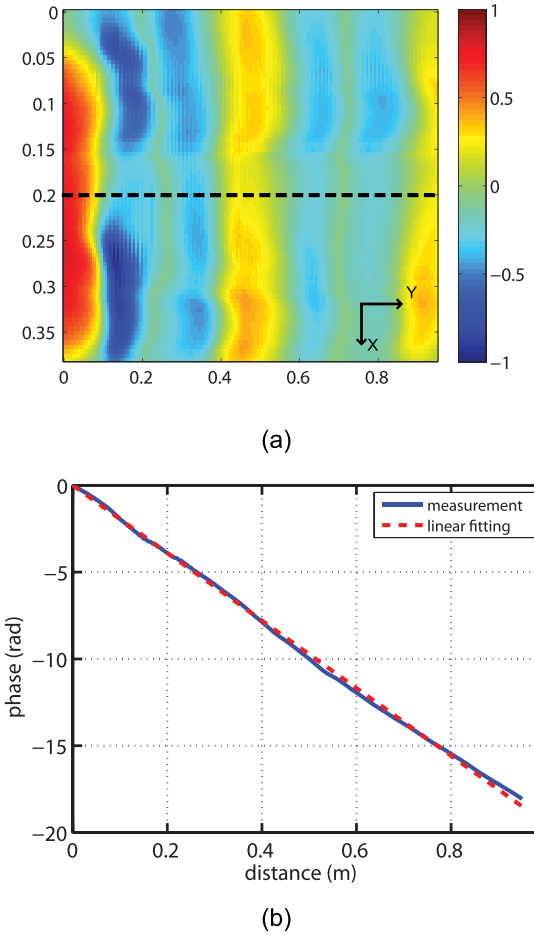

Fig. 9. Near-field measurement result. (a) Normalized near-field E_z distribution at 650 MHz. (b) Phase progression at the center (along the dashed line) is extracted. The first-order linear fit is applied to calculate its slope and further to derive the refractive index.

algorithm is used. Provided that the phase progression over this distance has a first-order linear fit coefficient, p_1, the propagation constant k and refractive index n are

$$k = -P_1 \tag{1}$$

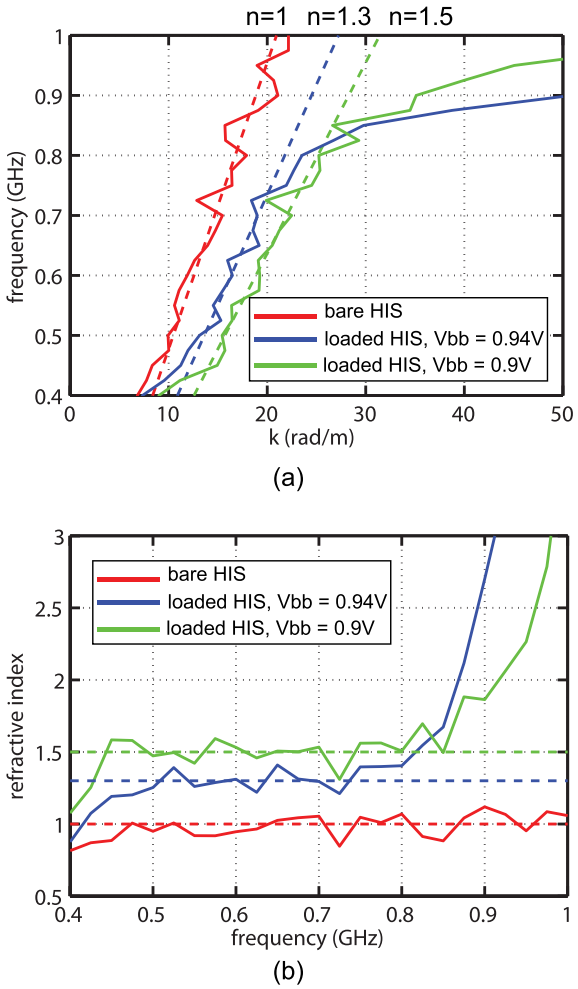

Fig. 10. Measured dispersion diagram and the measured refractive index. (a) Measured dispersion diagram of the bare impedance surface (red lines) and the non-Foster loaded surface at 0.94 V (blue lines) and 0.9 V (green lines). The ideal dispersion curve for $n = 1$, 1.3, and 1.5 are appended for comparison. (b) Refractive index versus frequency.

and

$$n = \frac{-P_1 \cdot c}{\omega} \tag{2}$$

where c is the speed of light. The surface impedance can be further found from the slow wave propagation index as [1]

$$Z_{\text{surf}} = \eta\sqrt{1 - n^2} \tag{3}$$

where $\eta = 377\ \Omega$ as the wave impedance in the free space. Thus, $n = 1.5$ is found for the extracted phase progression shown in Fig. 9(b), corresponding to $420\ j\Omega$. With the same manner, the refractive indices for frequencies from 400 to 1000 MHz are derived and summarized in Fig. 10. Below 400 MHz, it is hard to obtain an accurate phase since the 1-m-long impedance surface is still electrically short at low frequencies.

Fig. 10(a) presents the derived dispersion diagram for biasing of 0.9 (blue lines) and 0.94 V (red lines) respectively, which clearly shows that both $n = 1.3$ and $n = 1.5$ slow wave conditions have been realized. In particular, the consistency

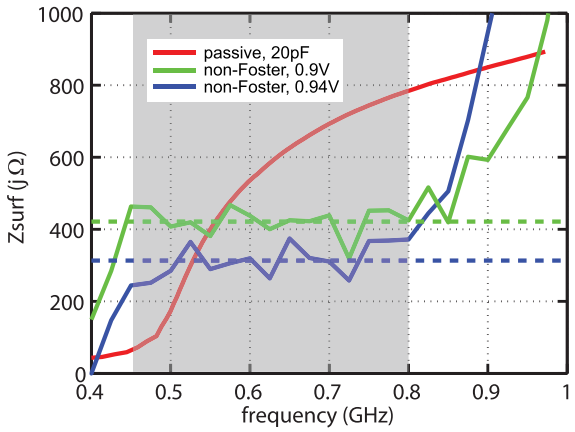

Fig. 11. Comparison of the impedance bandwidth obtained from passive (red curve) and non-Foster (blue and green curves) approaches.

with the ideal $n = 1.3$ and $n = 1.5$ line (dashed lines) for the measured dispersion curves (solid lines) over a wide bandwidth indicates that the accomplished slow wave propagation has low dispersion. The bare board without circuits populated is also measured, and the result is shown in Fig. 10(a) with red lines. It is found that the dispersion curve follows the light line over the entire frequency range below 1 GHz. As aforementioned, the unloaded surface is resonant at around 1.2 GHz. The consistency with the light line below 1 GHz is thus reasonable, confirming the measurement results. Ripples are observed for the measured dispersion curves. This is primarily due to the small size of the impedance surface sample compared with the wavelength. At UHF, all the measurement fixtures, including 2-D positioner, the surface wave launcher, and all other equipment in the same measurement environment, interact with the measured surface wave. A possible solution to obtain a stable phase progression is to measure a larger structure so that all the reflections can be sufficiently attenuated. Nevertheless, with the current limited-size surface, the overall performance, from 400 to 1000 MHz, clearly shows the predicted trends as expected.

Fig. 10(b) shows the refractive index versus frequency, which clearly manifests a wideband constant index of 1 (for unloaded surface), 1.3 (for the impedance surface with non-Foster load biased at 0.94 V), and 1.5 (for the surface with non-Foster load at 0.9 V). In particular, the achieved indices are constant over the bandwidth from 450 to 800 MHz, a 56% FBW.

The accomplished 450–800-MHz bandwidth is significant. Provided that the impedance surface is working at 450–800 MHz with the same 5-mm-thick surface having the same unit cell size loaded by a passive capacitor, based on Fig. 3, a 20-pF capacitor is needed, yet the bandwidth cannot be as large as what is achieved by the non-Foster impedance load. This can be seen from the comparison in Fig. 11, where the surface impedance of the non-Foster loaded surface (blue and green curves) are compared with the one obtained from a passive capacitance loaded surface (red curve). Within the shaded region (450–800 MHz), it is clear that the surface impedance achieved by the non-Foster load is much flatter, and covers much larger bandwidth than the passive loading approach. Although the non-Foster circuit increases the total thickness of the surface by 0.9 mm, the bandwidth increase is much larger than what can be achieved by merely thickening the surface by the same increment.

Regarding the scalability, the non-Foster loading approach can be theoretically applied at any frequency. However, the practical application may be limited by the non-Foster impedance implementation. There have been several papers reporting non-Foster circuits that can work up to several gigahertz [19], [21], [31]–[34]. Nevertheless, it is still an open question whether these applications can be realized at higher frequencies, which highly depends on the success of the non-Foster circuits.

VI. Conclusion

To sum up this paper, we have introduced a low-profile artificial impedance surface whose dispersion is significantly reduced over a wide bandwidth. The approach to accomplish this thin and nondispersive impedance surface is by loading a frequency-dependent non-Foster like impedance to the conventional electrically thin impedance surface unit cells. A non-Foster impedance, which is capable of reducing the dispersion of the artificial impedance surface, is found using a test capacitance, and the reduced dispersion of the non-Foster loaded surface is confirmed by both eigenmode and driven mode simulations. For experimental demonstration, the synthesized -2.8 pF $||$ -3.6 nH circuit is designed as a transistor-based NIC circuit and fabricated on the 5-mm-thick impedance surface structure in a back-to-back configuration, forming a multilayer impedance surface board. The fabricated non-Foster loaded artificial impedance surface is measured with the-near field scanner. From the near-field distribution, its surface impedance properties are characterized over a wide bandwidth. By extracting and analyzing the phase progression over the surface, constant slow wave propagation indices of 1.3 and 1.5 are measured over a bandwidth of 450–800 MHz, a 56% FBW. Compared with the passive capacitor loaded surface working in the same band, the non-Foster loaded artificial impedance surface possesses significantly larger bandwidth and less dispersion.

References

[1] D. F. Sievenpiper, "High-impedance electromagnetic surfaces," Ph.D. dissertation, Dept. Elect. Eng., UCLA, Los Angeles, CA, USA, 1999.

[2] D. F. Sievenpiper, L. Zhang, R. F. J. Broas, N. G. Alexópolous, and E. Yablonovitch, "High-impedance electromagnetic surfaces with a forbidden frequency band," *IEEE Trans. Microw. Theory Techn.*, vol. 47, no. 11, pp. 2059–2074, Nov. 1999.

[3] R. G. Quarfoth and D. F. Sievenpiper, "Nonscattering waveguides based on tensor impedance surfaces," *IEEE Trans. Antennas Propag.*, vol. 63, no. 4, pp. 1746–1755, Apr. 2015.

[4] R. Quarfoth and D. F. Sievenpiper, "Surface wave scattering reduction using beam shifters," *IEEE Antennas Wireless Propag. Lett.*, vol. 13, pp. 963–966, May 2014.

[5] H. Wakatsuchi, S. Kim, J. J. Rushton, and D. F. Sievenpiper, "Waveform-dependent absorbing metasurfaces," *Phys. Rev. Lett.*, vol. 111, no. 24, p. 245501, 2013.

[6] Z. Luo, X. Chen, J. Long, R. Quarfoth, and D. F. Sievenpiper, "Self-focusing of electromagnetic surface waves on a nonlinear impedance surface," *Appl. Phys. Lett.*, vol. 106, no. 21, p. 211102, 2015.

[7] R. F. J. Broas, D. F. Sievenpiper, and E. Yablonovitch, "A high-impedance ground plane applied to a cellphone handset geometry," *IEEE Trans. Microw. Theory Techn.*, vol. 49, no. 7, pp. 1262–1265, Jul. 2001.
[8] D. F. Sievenpiper, J. Schaffner, R. Loo, G. Tangonan, S. Ontiveros, and R. Harold, "A tunable impedance surface performing as a reconfigurable beam steering reflector," *IEEE Trans. Antennas Propag.*, vol. 50, no. 3, pp. 384–390, Mar. 2002.
[9] S. C. Chen, Y. S. Wang, and S. J. Chung, "A decoupling technique for increasing the port isolation between two strongly coupled antennas," *IEEE Trans. Antennas Propag.*, vol. 56, no. 12, pp. 3650–3658, Dec. 2008.
[10] F. Costa, S. Genovesi, and A. Monorchio, "On the bandwidth of high-impedance frequency selective surfaces," *IEEE Antennas Wireless Propag. Lett.*, vol. 8, pp. 1341–1344, Dec. 2009.
[11] F. Costa, A. Monorchio, and G. Manara, "Analysis and design of ultra thin electromagnetic absorbers comprising resistively loaded high impedance surfaces," *IEEE Trans. Antennas Propag.*, vol. 58, no. 5, pp. 1551–1558, May 2010.
[12] H.-J. Lee, K. L. Ford, and R. J. Langley, "Independently tunable low-profile dual-band high-impedance surface antenna system for applications in UHF band," *IEEE Trans. Antennas Propag.*, vol. 60, no. 9, pp. 4092–4101, Sep. 2012.
[13] C. Mias and J. H. Yap, "A varactor-tunable high impedance surface with a resistive-lumped-element biasing grid," *IEEE Trans. Antennas Propag.*, vol. 55, no. 7, pp. 1955–1962, Jul. 2007.
[14] D. J. Kern, D. H. Werner, and M. J. Wilhelm, "Active negative impedance loaded EBG structures for the realization of ultra-wideband artificial magnetic conductors," in *Proc. IEEE Antennas Propag. Soc. Int. Symp.*, vol. 2. Jun. 2003, pp. 427–430.
[15] J. Long, M. M. Jacob, and D. F. Sievenpiper, "Broadband fast-wave propagation in a non-Foster circuit loaded waveguide," *IEEE Trans. Microw. Theory Techn.*, vol. 62, no. 4, pp. 789–798, Apr. 2014.
[16] N. Zhu and R. W. Ziolkowski, "Active metamaterial-inspired broadbandwidth, efficient, electrically small antennas," *IEEE Antennas Wireless Propag. Lett.*, vol. 10, pp. 1582–1585, Dec. 2011.
[17] H. Mirzaei and G. V. Eleftheriades, "A wideband metamaterial-inspired compact antenna using embedded non-Foster matching," in *Proc. IEEE Int. Symp. Antennas Propag. (APSURSI)*, Jul. 2011, pp. 1950–1953.
[18] M. M. Jacob, J. Long, and D. F. Sievenpiper, "Non-Foster loaded parasitic array for broadband steerable patterns," *IEEE Trans. Antennas Propag.*, vol. 62, no. 12, pp. 6081–6090, Dec. 2014.
[19] P.-Y. Chen, C. Argyropoulos, and A. Alù, "Broadening the cloaking bandwidth with non-Foster metasurfaces," *Phys. Rev. Lett.*, vol. 111, no. 23, p. 233001, 2013.
[20] J. Long and D. F. Sievenpiper, "Stable multiple non-Foster circuits loaded waveguide for broadband non-dispersive fast-wave propagation," *Electron. Lett.*, vol. 50, no. 23, pp. 1708–1710, 2014.
[21] D. J. Gregoire, C. R. White, and J. S. Colburn, "Wideband artificial magnetic conductors loaded with non-Foster negative inductors," *IEEE Antennas Wireless Propag. Lett.*, vol. 10, pp. 1586–1589, Dec. 2011.
[22] M. Barbuto, A. Monti, F. Bilotti, and A. Toscano, "Design of a non-Foster actively loaded SRR and application in metamaterial-inspired components," *IEEE Trans. Antennas Propag.*, vol. 61, no. 3, pp. 1219–1227, Mar. 2013.
[23] F. Gao, F. Zhang, J. Long, M. Jacob, and D. F. Sievenpiper, "Non-dispersive tunable reflection phase shifter based on non-Foster circuits," *Electron. Lett.*, vol. 50, no. 22, pp. 1616–1618, 2014.
[24] J. Long and D. F. Sievenpiper, "Dispersion-reduced high impedance surface loaded with non-Foster impedances," in *Proc. IEEE AP-S Int. Symp.*, Vancouver, BC, Canada, Jul. 2015, pp. 69–70.
[25] S. Hrabar, I. Krois, and A. Kiricenko, "Towards active dispersionless ENZ metamaterial for cloaking applications," *Metamaterials*, vol. 4, nos. 2–3, pp. 89–97, 2010.
[26] R. M. Foster, "A reactance theorem," *Bell Syst. Tech. J.*, vol. 3, no. 2, pp. 259–267, Apr. 1924.
[27] J. G. Linvill, "Transistor negative-impedance converters," *Proc. IRE*, vol. 41, no. 6, pp. 725–729, 1953.
[28] S. D. Stearns, "Circuit stability theory for non-Foster circuits," in *IEEE MTT-S Int. Microw. Symp. Dig. (IMS)*, Jun. 2013, pp. 1–3.
[29] J. T. Aberle, "Two-port representation of an antenna with application to non-Foster matching networks," *IEEE Trans. Antennas Propag.*, vol. 56, no. 5, pp. 1218–1222, May 2008.
[30] S. D. Stearns, "Incorrect stability criteria for non-Foster circuits," in *Proc. IEEE AP-S Int. Symp.*, Chicago, IL, USA, Jul. 2012, pp. 1–2.
[31] S. Lee, H. Park, J. Kim, and Y. Kwon, "A 6–18 GHz GaN pHEMT power amplifier using non-Foster matching," in *Proc. IEEE MTT-S Int. Microw. Symp. (IMS)*, May 2015, pp. 1–4.
[32] S. Saadat, H. Aghasi, E. Afshari, and H. Mosallaei, "Low-power negative inductance integrated circuits for GHz applications," *IEEE Microw. Wireless Compon. Lett.*, vol. 25, no. 2, pp. 118–120, Feb. 2015.
[33] D. S. Nagarkoti, Y. Hao, D. P. Steenson, L. Li, E. H. Linfield, and K. Z. Rajab, "Design of broadband non-Foster circuits based on resonant tunneling diodes," *IEEE Antennas Wireless Propag. Lett.*, vol. 15, pp. 1398–1401, Apr. 2015.
[34] J. M. C. Covington, K. L. Smith, J. W. Shehan, V. S. Kshatri, T. P. Weldon, and R. S. Adams, "Measurement of a CMOS negative inductor for wideband non-Foster metamaterials," in *Proc. IEEE SOUTHEASTCON*, Mar. 2014, pp. 1–4.

Jiang Long (S'11) received the B.S. and M.S. degrees from Zhejiang University, Hangzhou, China, in 2007 and 2010, respectively. He is currently pursuing the Ph.D. degree with the University of California at San Diego, La Jolla, CA, USA.

His current research interests include non-foster circuits in antenna/microwave applications, including non-foster circuit loaded active fast-wave waveguides, broadband metasurfaces, broadband antennas, and active microwave components.

Mr. Long received the IEEE Microwave Theory and Techniques Society Graduate Fellowship in 2015.

Daniel F. Sievenpiper (M'94–SM'04–F'09) received the B.S. and Ph.D. degrees in electrical engineering from the University of California at Los Angeles, Los Angeles, CA, USA, in 1994 and 1999, respectively.

He is currently a Professor at the University of California, San Diego, La Jolla, CA, USA, where his research focuses on antennas and electromagnetic structures. Prior to 2010, he was the Director of the Applied Electromagnetics Laboratory at HRL Laboratories in Malibu, CA, USA, where his research included artificial impedance surfaces, conformal antennas, tunable and wearable antennas, and beam steering methods. He has more than 70 issued patents and more than 80 technical publications.

Dr. Sievenpiper was named as a Fellow of the IEEE in 2009. In 2008, he was awarded the URSI Issac Koga Gold Medal in 2008. Since 2010, he has served as an Associate Editor of IEEE *Antennas and Wireless Propagation Letters*.